Systematic Simulation Strategy of Plasma Methane Pyrolysis for CO$_2$-Free H$_2$

Aliya Magazova[1],*, Simon Böddeker[2], Nikita Bibinov[2], and David W. Agar[1]

Supporting Information available online

Recently, the direct conversion of methane into hydrogen using cold plasma reactors has attracted increasing attention, since hydrogen has considerable potential as a future feedstock in the steel and chemical industries. However, the simulation of plasma pyrolysis reactors is extremely complex due to the vast temporal and spatial ranges of the variables involved and steep gradients. Previously, methane pyrolysis has been meticulously modeled by 0D simulations, and 3D plasma modeling has been largely confined to Argon systems. In this paper, a systematic methodology is presented, which provides an expedient and efficient hierarchy of 0D to 3D simulations, in order to approximate the methane pyrolysis simulation of a plasma reactor in its entirety. Various simulation tools are applied in a coordinated and pragmatic manner. The results show that the proposed synergy allows simplification of the reaction set and arc characteristics, significantly reducing the runtime required for the simulations.

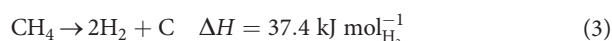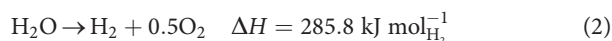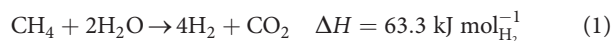**Keywords:** CFD simulation, Hydrogen, Methane pyrolysis, Plasma

Received: September 30, 2021; *revised:* February 18, 2022; *accepted:* March 11, 2022

1 Introduction

In order to tackle anthropogenic climate change green energy technologies are receiving increasing attention [1]. The share of renewable sources of energy for electricity production is growing by leaps and bounds, while the use of fossil fuels as energy source is stagnating, or even diminishing. Nevertheless, the utilization of natural gas is still significant and rising [2]. By virtue of the extensive proven reserves of natural gas, methane can serve as a low- or even zero-carbon transitional bridging fuel to green energy [3]. Methane can be converted to CO$_2$-free hydrogen if renewable energy is used to drive the pyrolysis process generating only hydrogen and carbon.

Despite hydrogen itself being colorless, hydrogen manufacture is color-coded according to the environmental impact of its production. The prevalent industrial route for hydrogen production from methane is via methane steam-reforming (Eq. (1)). When the CO$_2$ by-product of this process is released into the atmosphere, such hydrogen is referred to as gray [4]. Gray hydrogen becomes blue when CO$_2$ emissions are drastically cut by means of carbon capture and storage (CCS). Such reduction is of course desirable, but CCS is still technically immature and geologically controversial [5]. Hydrogen produced from water electrolysis powered by renewable energy (Eq. (2)) is completely car-

bon-neutral and thus designated as being green. A recent addition to this hydrogen color scheme is turquoise hydrogen, which is manufactured by methane pyrolysis as shown in Eq. (3). If the energy supply for the pyrolysis is renewable the process is carbon-neutral, since only solid carbon and no CO$_2$ is formed [4]. Fig. 1 depicts the summary of the mentioned hydrogen. Further hydrogen color-codes, such as black, purple, red, have also been assigned according to the exact feedstock and energy source used.

$$CH_4 + 2H_2O \rightarrow 4H_2 + CO_2 \quad \Delta H = 63.3 \text{ kJ mol}_{H_2}^{-1} \quad (1)$$

$$H_2O \rightarrow H_2 + 0.5O_2 \quad \Delta H = 285.8 \text{ kJ mol}_{H_2}^{-1} \quad (2)$$

$$CH_4 \rightarrow 2H_2 + C \quad \Delta H = 37.4 \text{ kJ mol}_{H_2}^{-1} \quad (3)$$

[1]Aliya Magazova, Prof. Dr. David W. Agar
aliya.magazova@tu-dortmund.de
Technische Universität Dortmund, Lehrstuhl für Chemische Verfahrenstechnik, Emil-Figge-Straße 66, 44227 Dortmund, Germany.
[2]Simon Böddeker, Dr. Nikita Bibinov
Ruhr-Universität Bochum, Lehrstuhl für Allgemeine Elektrotechnik und Plasmatechnik, Universitätsstraße 150, 44801 Bochum, Germany.
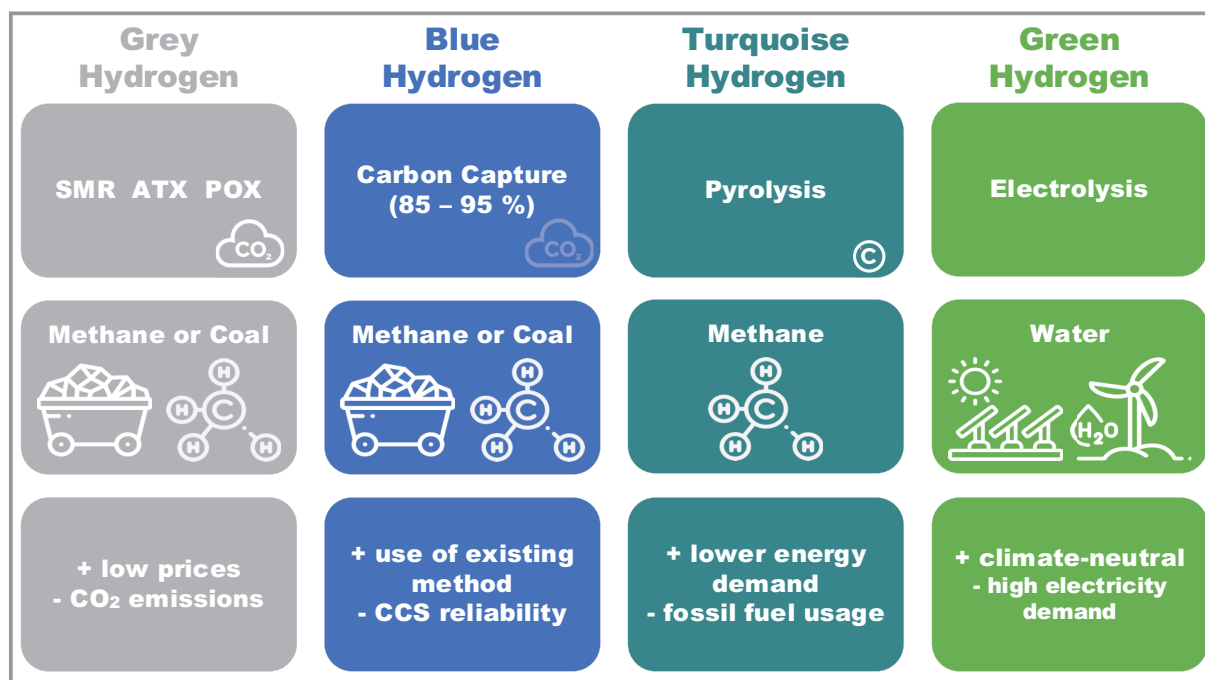
Figure 1. Scheme of plasma reactor integration.

Although green hydrogen offers environmental advantages over the turquoise variety, because it involves no fossil fuels, the reaction enthalpies in Eq. (2) and (3) indicate that the energy demand for electrolysis is several times higher than in for methane pyrolysis, making the latter an economically a more attractive option.

One way to implement methane pyrolysis is by using plasma. In such reactors the energy demand of the pyrolysis is supplied by electricity. The electric energy ignites the plasma, which then splits CH_4 into its elements and other valuable by-products. Electrical energy also enables flexible reactor operation since the start-up and shutdown are quicker than for thermal pyrolysis processes. The production of hydrogen can therefore be readily adjusted to the availability of renewable electricity. As shown in Fig. 1, surplus electricity from the grid can thus be valorized as hydrogen and other value-added chemicals. In the plasma generated, the reaction medium comprises electrons and ions together with various reactive and neutral species, all of which may react with one another. Electrons in plasma react with other species through elastic collisions with the transfer of kinetic energy. There are also excitation reactions, in which the electron energy of neutral particles is increased and ionization reactions, which displace an electron from the outer shell of a neutral species. Additionally, heavy species react and combine with each other without introduction of thermal energy. The reactions can therefore take place at lower temperatures and within smaller volumes [6].

Plasma is generated by injecting sufficient amounts of energy into a gas. The most common way to supply this energy is by an electric field, which is either constant (DC), an alternating at low (AC) or radio frequencies (RF), or by using electromagnetic radiation at GHz frequencies [7, 8]. Plasma is generally categorized as being thermal or nonthermal. The former is characterized by thermal equilibrium between all species meaning that the electron and gas temperatures, which can be as high as 10^4 K, are equal. Thermal plasmas are almost fully ionized and thus exhibit a high charge density. Nonthermal plasma is distinguished by a large difference in temperature between the electrons and the ions. With the electron temperature being at several thousand Kelvin, whilst the gas and ions usually remain at room temperature [9, 10].

Plasma processes have a wide range of applications. For instance, they are used in processes for waste disposal, surface coating, medicine and in microelectronics [7]. More recently, potential, applications in the chemical industry have attracted interest, e.g., processes for the conversion of gases such as carbon dioxide [11] and methane [12] have been investigated. In particular, nonthermal plasma has been the focus of such work, because the electrical energy is largely converted into electrons and so the plasma can easily reach high electron temperatures without having to heat up the entire gas, resulting in improved energy efficiency [13]. Thanks to the low gas temperature, the investment in equipment is also lower, because the harsh conditions are avoided.

Several types of plasma have already been studied for methane pyrolysis [14]. In this study only the nonthermal gliding-arc plasma (GAP) is considered. In GAP, a high voltage is applied between two electrodes, whereupon the

gas ionizes and becomes conductive. The ionization of the gas goes through several phases. First, there is a so-called Townsend discharge, followed by a glow discharge, up to the point where the ionization is sufficient to trigger an arc discharge. This arc discharge is then denoted as a plasma arc [15].

The simulation of such plasma reactors is a non-trivial problem, but is nevertheless essential, since the simulation results help to validate and verify theories that cannot be resolved by experiments alone, enable one to optimize the reactor design and operating conditions and to save time and effort. However, there are a few major challenges that need to be surmounted, such as dealing with the high gradients of variables, since the temperatures vary between atmospheric conditions and thousands of Kelvins, the wide range of time scales between reactions occurring within microseconds and the residence times measured in seconds, and the complexity of interactions between turbulent flow and the plasma. In previous attempts to simulate CH_4 conversion in GAP 0D simulations as in [16, 17] were mainly employed to elucidate the reaction kinetics. Although 2D [18] and 3D [19] simulations were used to reproduce actual plasma behavior, they were confined to argon gas to render the plasma simulations manageable, due to the much simpler reaction scheme than with methane. However, this approach leads to an unsatisfactory hodgepodge of 0D, 2D and 3D simulations with considerable leaps of faith between them. In this paper we propose a streamlined technique to solve this simulation conundrum in just few steps using various simulation tools as appropriate, in order to obtain the results sought for the whole reactor in a relatively short amount of time.

2 0D Modeling

Plasma chemistry is generally a complicated process, where a large number of reactions take place simultaneously. The reactions may be classified as electron impact reactions and thermal reactions. The thermal reactions are those between neutral species, with the reaction rate constant being dependent on the gas temperature as given by the Arrhenius equation in Eq. (4):

$$k_j = A_i T_g^{n_i} \exp\left(-\frac{E_{Ai}}{RT_g}\right) \tag{4}$$

where A_i is the frequency factor and E_{Ai} is the activation energy.

On the other hand, the rate coefficients of electron impact reactions are a function of the electron temperature, and this function is in turn dependent on the electron energy distribution functions (EEDF) [20]. The EEDF is the probability distribution function for an electron energy and can be described as a Maxwellian, Druyvesteyn or generalized function or be computed by solving the Boltzman equation.

In most of the simulations EEDF is assumed to possess a Maxwellian form and the rate coefficients are calculated by integrating the cross-sectional data over the EEDF as shown in Eq. (5):

$$k_j = \int_{\varepsilon_{th}}^{\infty} \sigma_j(\varepsilon_e)\nu(\varepsilon_e)f(\varepsilon_e)\mathrm{d}\varepsilon_e \tag{5}$$

where ε_e is the electron energy (eV), ε_{th} is the threshold energy required to start the reaction, $\sigma_j(\varepsilon_e)$ is the cross-sectional data for the electron impact reaction j (m^2), $\nu(\varepsilon_e)$ is the velocity of the electrons ($m\,s^{-1}$) and $f(\varepsilon_e)$ is the normalized EEDF (eV^{-1}).

As a first step, a 0D modeling is carried out, which includes the methane (CH_4) pyrolysis reactions. A 0D model is based on solving the species balance equations given by Eq. (6) for all the number densities of the species, including the reactive sink and source terms. It only yields the temporal evolution of the species, whilst their concentrations are averaged over the reaction space.

$$\frac{\mathrm{d}n_i}{\mathrm{d}t} = \sum_j \left\{ \left(a_{ij}^{(2)} - a_{ij}^{(1)}\right) k_j \prod_l n_l^{a_{ij}^{(1)}} \right\} \tag{6}$$

where $a_{ij}^{(1)}$ and $a_{ij}^{(2)}$ are the i-species' stoichiometric coefficients on the right- and left-hand side of the reaction j, n_1 is the number density of the species on the left-hand side, k_j is the rate coefficient of the reaction j. To solve the 0D model, a commercial software COMSOL Multiphysics™ was used, since its user-friendly interface and the built-in BOLSIG+ solver enables one to obtain the results quickly. Due to the fact that only temporal and no spatial variation is considered, it is possible to simulate several hundred simultaneous reactions in a short time and without needing exceptional computing power.

In this way it was possible to observe the effect of plasma carrier gas on the products being formed. It should be noted that the carrier gas is mainly used to ignite and sustain the plasma, with argon (Ar), nitrogen (N_2) and hydrogen (H_2) often being used for this purpose. In Fig. 2 and 3, various mixture composition of methane and argon were simulated, with reaction rates taken from literature [16, 21–26] and the list of reactions is summarized in Tab. S1 in the Supporting Information (SI). Both cases were simulated over a period of 10 ms, which is sufficient for 0D since the reactions occur almost instantaneously. Moreover, the gas composition attained a steady state, so that it would not be expected that lengthening the simulation time would result in a different outcome. It was also assumed that the gas temperature is constant at around 2000 K, which is based on the available literature [27].

Changing the carrier gas concentration shows that increasing the CH_4 level in the mixture results in greater H_2 production, which is hardly surprising, since more reactant is being fed into the reactor. However, it is noticeable that
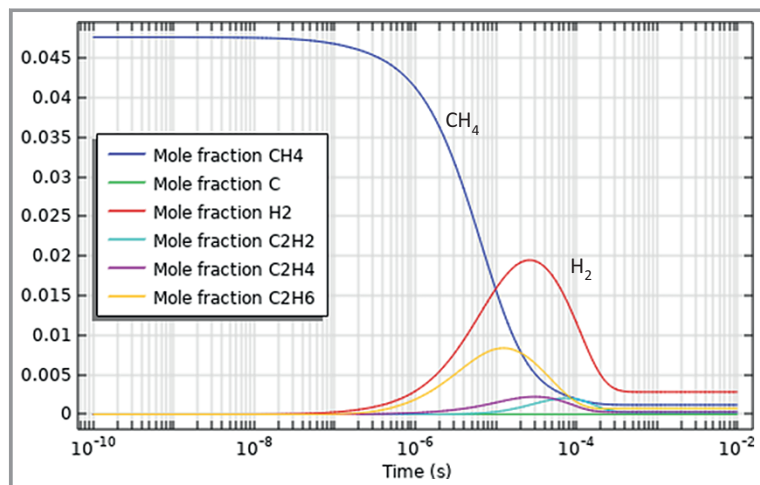
Figure 2. Calculated mole fractions for CH_4:Ar ratio of 1:20 at T_g = 2000 K and 1600 V discharge.
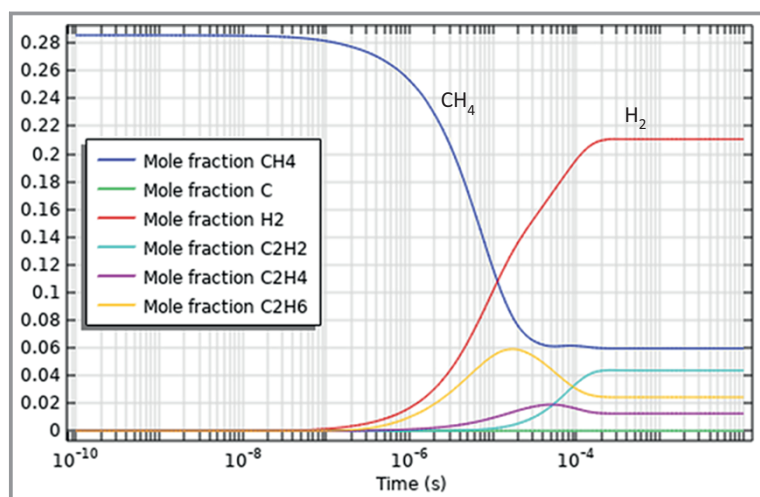

Figure 3. Calculated mole fractions for CH_4:Ar ratio of 6:15 at T_g = 2000 K and 1600 V discharge.

the conversion of methane tails off with increasing methane composition in the feed, which can be explained by the fact that CH_4 molecules are heavier than Ar, and thus require more energy to be cleaved into radicals and react further. Another interesting phenomenon is that H_2 is generated and consumed in the bell-shaped curve in Fig. 2, whereas in Fig. 3, H_2 constantly rises until reaching the steady-state value. There are few intermediate reactions where H_2 serves as a reactant, hence, when the rate of consumption of H_2 exceeds the rate of generation, less H_2 is produced. It is evident that with increasing amounts of CH_4 in the feed, the intermediate reactions have less impact on H_2 production. Therefore, a more favorable feed composition can be selected on the basis of the 0D modeling results.

As mentioned before, different gases can be utilized as the plasma carrier gas. Thus, nitrogen was also examined as a carrier gas. The reactions simulated are listed in Tabs. S3,

S5–7 in the SI. Fig. 4 illustrates the number density profile, with the reaction kinetics taken from literature [28]. A major concern with N_2 as carrier gas is the possible formation of toxic HCN, which needs to be clarified when planning experiments.

For the simulation results based on the literature kinetics, Fig. 4 indicates that along with the target product H_2 and valuable by-product hydrocarbon C_2H_2, a significant amount of HCN is generated, at molar fractions of up to around 2 mol %. For safety-reasons argon is thus to be preferred over nitrogen as a carrier gas in experimental work.

Another example showing how 0D modeling in COMSOL Multiphysics™ could be useful is for the refinement of the reaction set for methane pyrolysis in a plasma. To reduce the subsequent computational effort for 2D or 3D simulations. Hence the relative contributions of the electron impact reactions versus thermal reactions for CH_3 radical generation was compared, since this radical represents a key starting point for further reactions. Fig. 5 and 6 depict the evolution of the product spectrum over time, with the reaction kinetics taken from the literature [14, 29] (the reactions are given in Tabs. S2–S4). In Fig. 5 the operating temperature is set to 3000 K, and in Fig. 6 to 300 K.

Comparing Fig. 5 and 6, independent of the temperature, H_2 remains the dominant product, but the fractions of the valuable by-products C_2H_2 and C_2H_4 are reversed. This is because C_2H_4 is mainly converted into C_2H_2 at high temperatures, whereas at lower temperature, this reaction is less active. This observation suggest how one might manipulate the type of C_2 hydrocarbons generated by tuning the gas temperature, which is dictated by the power supply.

Some of the reactions in which CH_3 radicals $\left(CH_3^\bullet\right)$ are generated are listed in Eq. (7)–(10):

$$CH_4 + H^\bullet \rightarrow CH_3^\bullet + H_2 \tag{7}$$

$$CH_2 + H_2 \rightarrow CH_3^\bullet + H^\bullet \tag{8}$$

$$CH_4 \rightarrow CH_3^\bullet + H^\bullet \tag{9}$$

$$e + CH_4 \rightarrow e + CH_3^\bullet + H^\bullet \tag{10}$$

At 300 K, the thermal reactions are negligible, and CH_3 radicals are formed exclusively from electron impact reaction (Eq. (10)). At 3000 K, both thermal and electron impact reactions are significant, but the CH_3 radical is primarily being produced by the thermal reaction (Eq. (7)). Tab. 1 summarizes the above-mentioned quantitative differences by listing the reaction rates for 300 K and 3000 K.
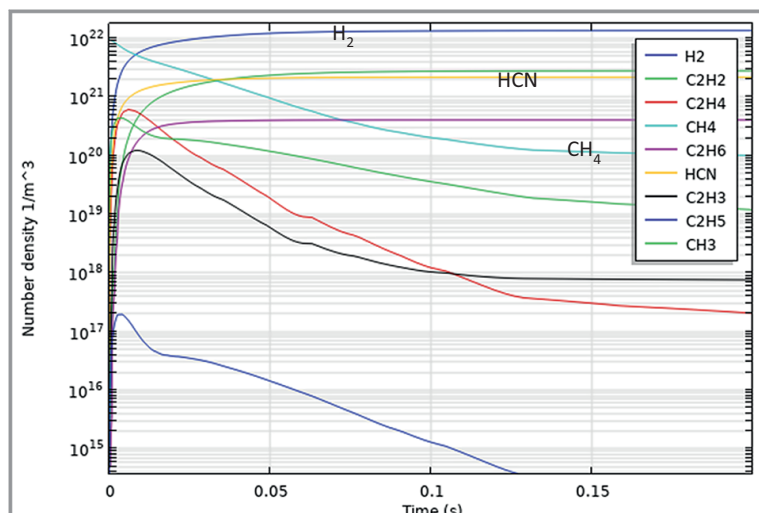
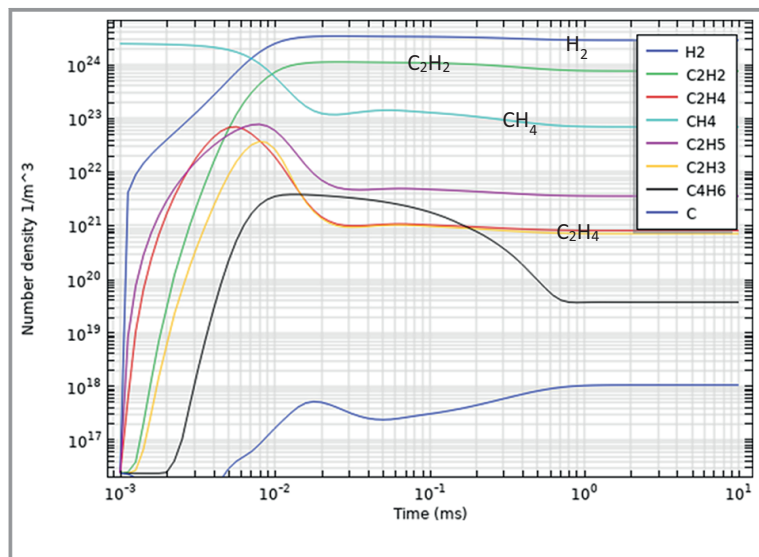**Figure 4.** Calculated number densities for CH$_4$-N$_2$ mixture with 1:5 ratio, at 2000 K.

Figure 5. Calculated number densities for pure CH$_4$ at 3000 K.

Table 1. Calculated production rate of $\left(CH_3^{\bullet}\right)$ at 300 K and 3000 K for the selected reactions.

Reaction number	Production rate [mol m^{-3}s^{-1}]	
	300 K	3000 K
Eq. (7)	$2.67 \cdot 10^{-6}$	1.5806
Eq. (8)	0.0004	0.0015
Eq. (9)	$3.36 \cdot 10^{-66}$	0.0016
Eq. (10)	0.014	0.0019

Thus, for 2D or 3D plasma reactor simulations, given that the experiments indicate high gas temperatures in the arc, the electron impact reactions can be neglected.

0D modeling is therefore advantageous for understanding the plasma chemistry, allowing one to rationally reduce the reaction set and to observe the influence of parameters such as the power supply, feed composition, temperature and so on in a series of rapid screening simulations. However, the spatial variation of the species concentrations required for reliable simulation of the reactor are still lacking, a deficit that will be addressed in the following sections.

3 2D Modeling

The objective of the 2D modeling stage is to simulate the arc and to observe how it moves and interacts with the gas flow and thus identify where the reactive zones are located. For this purpose, an open-source simulation tool Open-FOAM$^{®}$ was used instead of COMSOL Multiphysics$^{™}$. OpenFOAM$^{®}$ is generally referred to as a software package for numerical flow simulation [30]. Since it is C++ based, the source code is directly accessible, and the model equations for the calculations can be introduced, modified and extended manually.

The 3D simulation of the fluid flow is a complicated task in its own right and incorporating additional plasma chemistry makes it even more computationally intensive. Therefore, a simple reactor geometry in 2D is first considered to simulate the gliding arc plasma. Such a simplification was inspired by [18], where the gliding arc was dealt with using a Cartesian model. However, the results could not be replicated in COMSOL Multiphysics$^{™}$, so OpenFOAM$^{®}$ was employed instead. In addition, argon chemistry is substituted for the methane pyrolysis reactions, to facilitate the computation. Such 2D simulation, nevertheless, helps to identify important plasma physics equations, which can then be used in 3D simulations of real reactor geometries. Fig. 7 shows the reaction zone that is formed from two curved electrodes with narrow gap in the middle. The gas is flowing in the upward vertical direction as indicated by the velocity arrow vectors in Fig. 7a. A jet flow is created with accompanying vortices on both sides. As for the pressure, which is illustrated in Fig. 7b, the lower part of the reactor is at a uniformly higher pressure compared to the upper section. The high-pressure zone is separated from the low-pressure zone at the throat of the reactor. However, for the plasma simulation, the pressure field was neglected and considered constant over the entire reactor.

Several methods exist to calculate the temporal and spacial evolution of plasma. For instance, Monte-Carlo simulation based on statics, kinetic methods that involve solving
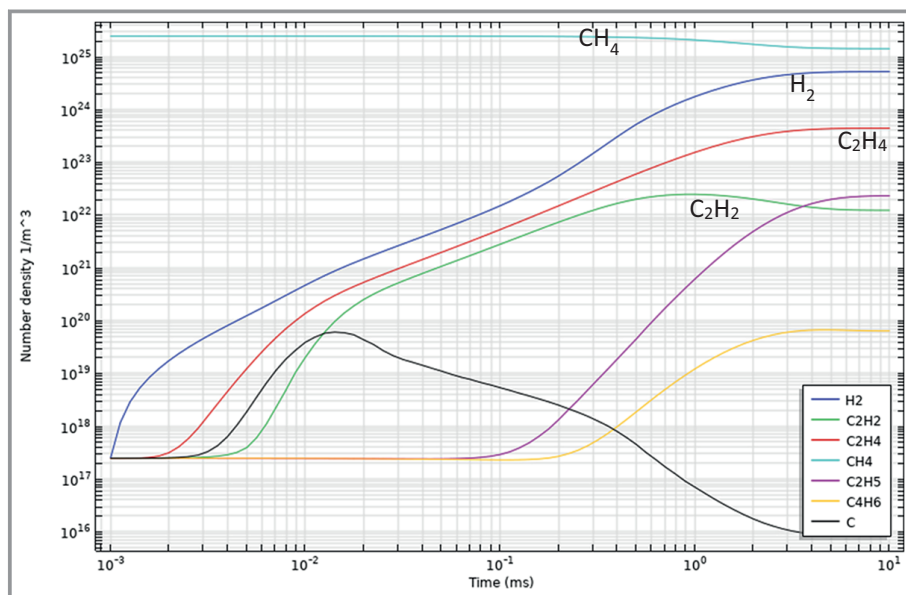
Figure 6. Calculated number densities for pure CH$_4$ at 300 K.

where Γ_i is the flux, $(u_{gas}\nabla)n_i$ is for the species carried in the gas, and S_i is the source term of species i.

The ion and electron fluxes are calculated by means of Eq. (12) and (13):

$$\Gamma_{ion} = -\frac{n_{ion}}{v_{ion}}$$

$$\times (v_{ion}\nabla)v_{ion} \pm \mu_{ion}En_{ion} - D_{ion}\nabla n_{ion} \quad (12)$$

where the first term on the right-hand side represents the collision frequency, the next one the mobility of the ions in the electrical field and the final one gives the diffusion term.

$$\Gamma_e = -\mu_e En_e - D_e\nabla n_e \quad (13)$$

the Boltzmann equation and particle-in-cell simulations. All of these methods are very time consuming, so that an alternative fluid-plasma model was applied here, in which different species in the plasma are considered as fluid, necessitating the solution of the following balance equations (Eq. (11)) [31, 32].

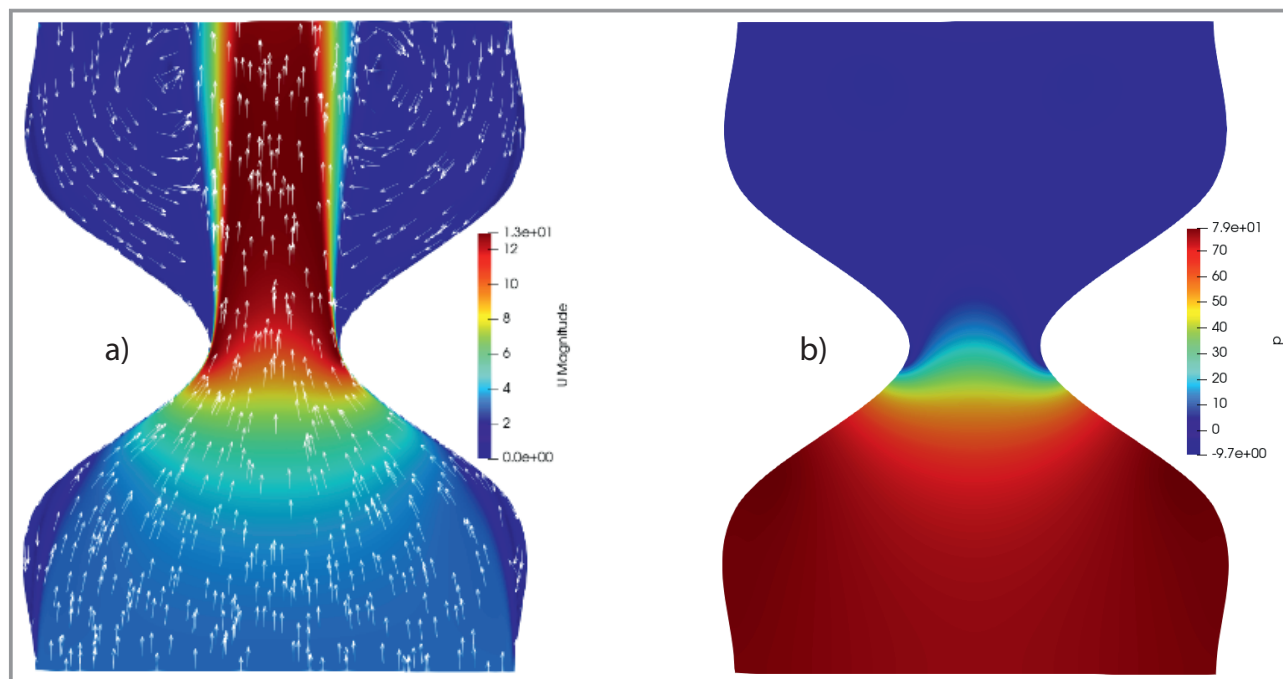$$\frac{\partial n_i}{\partial t} + \nabla\Gamma_i + (u_{gas}\nabla)n_i = S_i \quad (11)$$

The mobility and the diffusion are obtained from Eq. (14) and (15):

$$\mu = \frac{q}{mv} \quad (14)$$

where q is the charge, m is the mass, and v is the elastic collision frequency,

Figure 7. a) Velocity (m s^{-1})(a) and b) pressure field normalized over density (Pa m^{3}kg^{-1}) of the arbitrary geometry in 2D.

$$D = \frac{k_B T}{mv} \qquad (15)$$

where k_B is the Boltzmann constant, and T is the temperature.

Additionally, the average energy density of the species $n_i \varepsilon_i$ should be calculated from the energy balance (Eq. (16)).

$$\frac{\partial n_i \varepsilon_i}{\partial t} + \nabla \Gamma_{\varepsilon i} \mp q_e E \Gamma_{\varepsilon i} + \Theta_i + (u_{gas} \nabla) n_{\varepsilon i} = Q_{\varepsilon i} \qquad (16)$$

where $\mp q_e E \Gamma_{\varepsilon i}$ term represents the power discharge transmitted through the electric field, Θ_i is the power lost in collisions, $Q_{\varepsilon i}$ is the external energy source.

According to the operating principle of the gliding arc plasma, the arc ignites at the smallest separation between the electrodes and moves in the direction of gas flow. Fig. 8a depicts the arc position via the electron density at the start of the simulation and Fig. 8b shows the arc development after 600 μs.

In Fig. 8b the electron and ion density rises due to plasma growth, and the plasma arches visibly upward as a consequence of gas flow and the diffusion of itself. The simulation results are in accordance with experimental observations from the literature [33].

The electron temperature should also be considered since it is directly coupled with the gas temperature. Fig. 9a shows the electron temperature profile at the start of the simulation and Fig. 9b at the end of it.

The electron temperature is highest at the arc location, and with time the high values of the electron temperature spread following the expansion of the plasma region. This expansion also indicates that the relevant reaction zone becomes larger.

Correspondingly, the gas temperature is illustrated in Fig. 10. The gas temperature is high at the location of the arc, whereas the rest of the gas remains at ambient temperature (Fig. 10b). The simulation thus exhibits the characteristic nonthermal plasma behavior of the gliding arc.
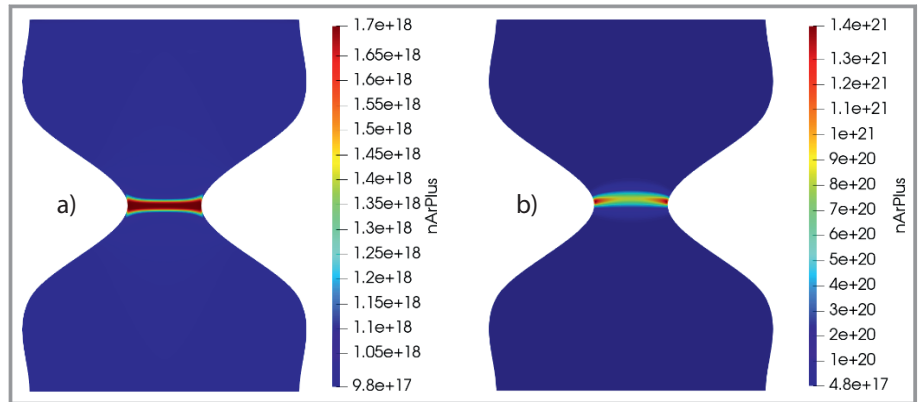

Figure 8. Number density (m^{-3}) of Ar$^+$ respectively e for a) $3 \cdot 10^{-6}$ s and b) $6 \cdot 10^{-4}$ s.
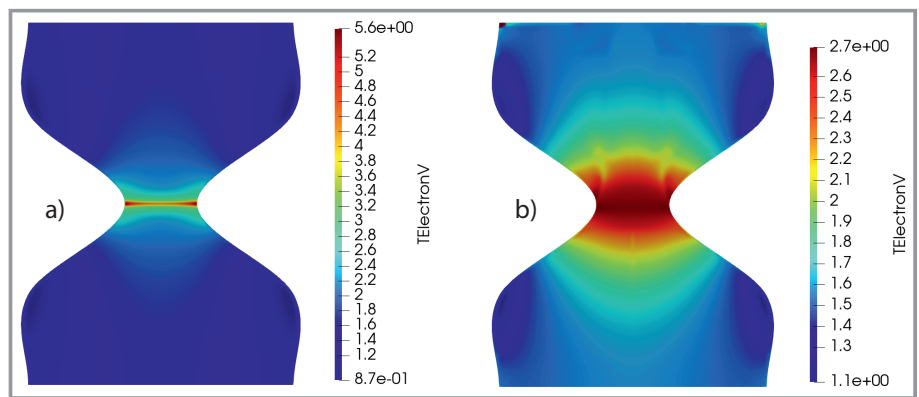

Figure 9. Electron temperature for a) $3 \cdot 10^{-6}$ s and b) $6 \cdot 10^{-4}$ s.
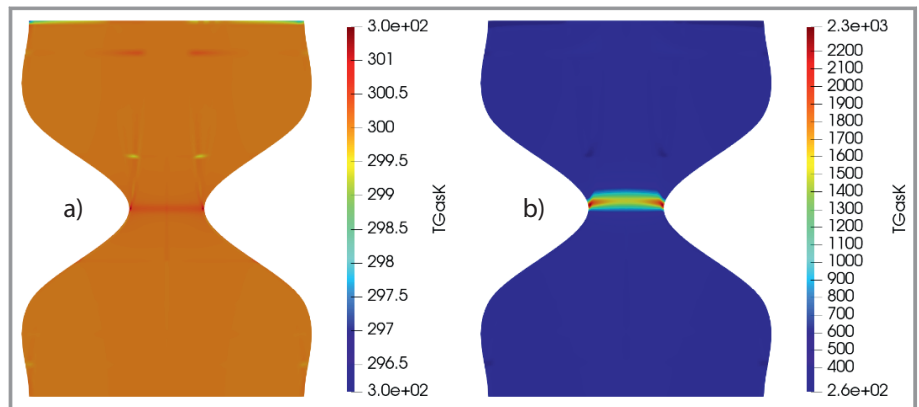

Figure 10. Gas temperature for a) $3 \cdot 10^{-6}$ s and b) $6 \cdot 10^{-4}$ s.

The simulation of the arbitrary 2D geometry with Ar chemistry allows on to identify a set of equations portraying and localizing the plasma arc. This was possible due to use of OpenFOAM®, where the user has a great control over the depth of modeling and can observe and post-process the results during the simulation run and not only at the end of the run, as with COMSOL Multiphysics™. However, the disadvantage of OpenFOAM® is that the software is less user-friendly and requires a higher degree of software expertise.

© 2022 The Authors. Chemie Ingenieur Technik published by Wiley-VCH GmbH

4 3D Modeling

Having discussed the 0D and 2D modeling of the plasma reactor, the following section is devoted to the 3D simulation strategy. Despite its complexity, 3D simulation is indispensable for acquiring a complete picture with respect to gas flow, heat transfer and reactant conversion.

A photo of an experimental GAP located at the Ruhr-Universität Bochum is shown in Fig. 11 a while Fig. 11b provides the frontal view of the plasma arc. The arc forms between the cathode cap and anode tube. Although it seems in Fig. 11 a as though one end of the arc is disconnected and emerging outside of the reactor, in reality the loop of the arc is visible at the exit of the reactor. The arc rotates due to vortex motion of the gas, where the vortex is created by the tangential inlets between the cathode cap and anode tube, with the gas flowing out of the anode tube. Depending on the gas velocity, mixture composition, power supply and reactor geometry, the arc properties such as electron density, temperature and plasma volume vary.

Since simulation of the plasma in 3D is a complicated and time-consuming process, few simplifications were adopted. Firstly, the arc shape is assumed to be less chaotic and have a more regular, straighter shape (Fig. 12a). Secondly, the plasma arc is substituted by a heat source. From the 2D simulations it was demonstrated that the gas temperature at the arc location reaches a few thousand Kelvin and from 0D simulation it is known that at high temperatures the influence of electron impact reactions diminishes, and the thermal reaction mechanism prevails.

The arc substitution employed thus seems reasonable. In the dynamic simulation, the heat source is manually rotated inside the reactor with the same speed as the gas. The resulting temperature fields are given in Fig. 12, with Fig. 12a depicting a 2D plane section of the reactor in side view. The snapshot also illustrates the current and previous location of the arc by the two vertical hot regions. in conformity with the properties of the gliding arc, where only the arc is heated, and the rest of the gas remains at ambient conditions. Fig. 12b, where the 2D section viewed from above is shown, suggests that the reactor walls are not heated up owing to the gas vortex motion. Fig. 12c shows a 3D contour plot of the temperature in the reactor, where the colored volume indicates the path of the arc. This 3D dynamic simulation was carried out in OpenFOAM®, because the solving time is shorter and the solvers are more robust.

Such 3D simulation can be of assistance in identifying reactor hot spots, as well as the velocity and power supply limitation. In the laboratory, it is difficult to introduce tracers or
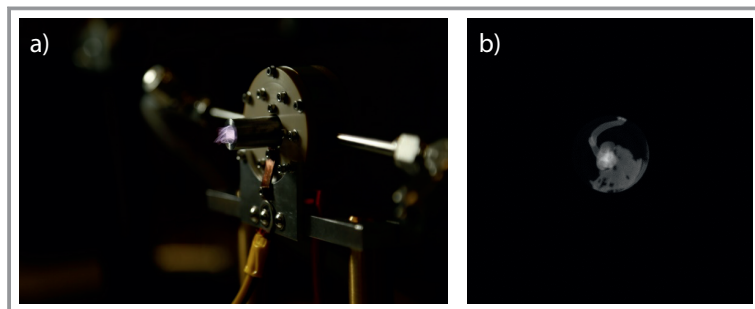

Figure 11. a) Gliding arc plasma reactor and b) the front view of the arc [30].
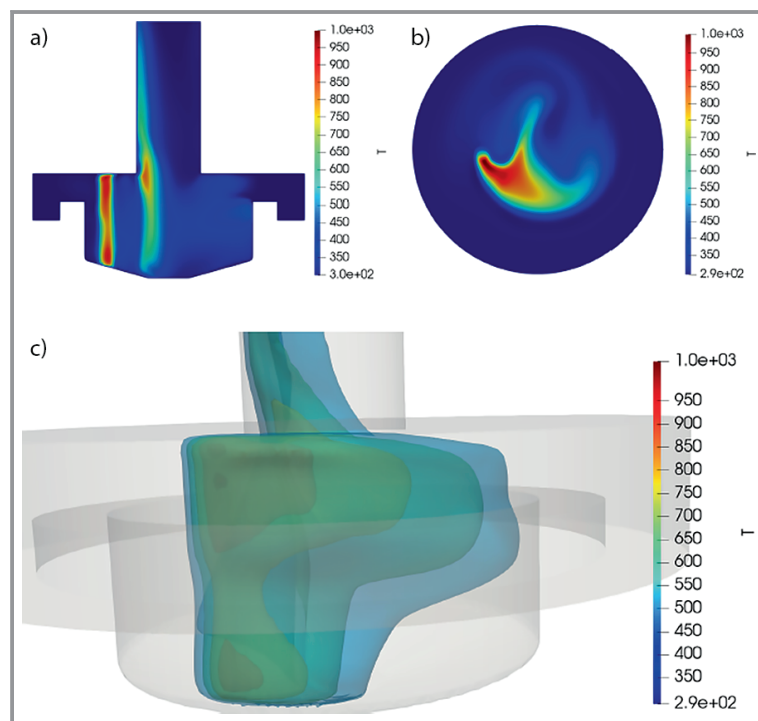

Figure 12. Temperature magnitude in 2D cut (a), top view (b) and in 3D (c) with contours of the temperature field.

thermocouples directly inside the reactor, because the plasma arc is sensitive to disturbances, and gives rise to exceedingly high temperatures. The 3D simulations therefore also help to elucidate the laboratory observations. In Fig. 13 the velocity arrow plot and the corresponding streamlines are shown for two different reactor inlet diameters of 1 and 2 mm.

During the experiments with 1 mm inlet diameter, the arc shift towards the middle of the reactor was hindered, and the reactor flow was chaotic, whereas with 2 mm inlet diameter, the arc could be generated at the smallest distance between the electrodes and migrated to the center of the reactor. The streamlines are smoother with the larger inlet diameter, while with the smaller diameter gives rise to more eddies at the location where the arc is supposed to ignite. The simulations can thus be used to justify increase of the inlet diameter [34].
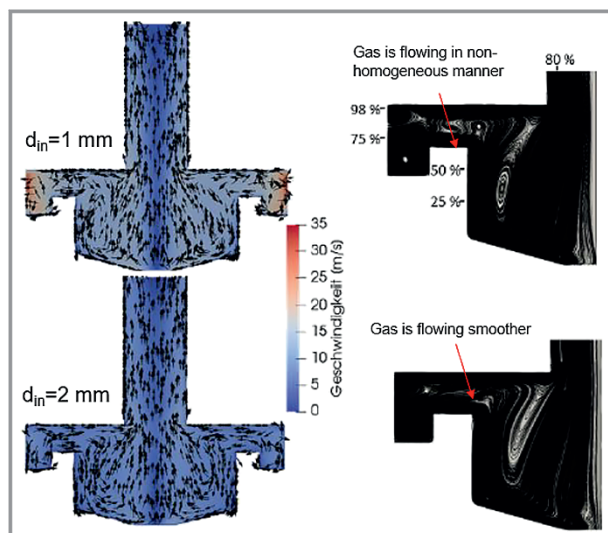
Figure 13. Velocity arrow plot and streamlines for 1 and 2 mm diameter.

5   Software Comparison

Several software packages were used in the bottom-up approach presented here for the sequential 0D to 3D modeling of the plasma pyrolysis reactor for methane conversion into hydrogen. Tab. 2 summarizes the applicability of the various software in the different contexts. The software used was COMSOL Multiphysics™, Ansys Fluent®, and OpenFOAM®. The simulation results in Ansys Fluent® are not presented in this paper, however, it is widely used in the industry and was also employed for certain of the reactor simulations.

For 0D modeling and simulation, COMSOL Multiphysics™ offers a good set of built-in functions, which permits a less time-consuming evaluation of the plasma chemistry. In 2D simulations, COMSOL Multiphysics™ has convergence issues, and the simulation conditions need to be tuned carefully. With OpenFOAM® on the other hand, the simulation solution is more flexible and rapid due to the nature of the software. Ansys Fluent® can also be used for 2D simulations, however, the simulation requires the adjustments to the problem posed. For 3D modeling, both Ansys Fluent® and OpenFOAM® resulted in the less time-consuming simulations. While COMSOL Multiphysics™ had convergence issues in 3D simulation, even with the simplifications made to the plasma. Generally, the insights into

the process within a relatively limited time frame can best be obtained through the judicious combination of software described here, exploiting the strengths of the various packages and integrating them over well-defined boundaries.

6   Conclusion

CO_2-free hydrogen can be manufactured economically and in an environmentally friendly manner from methane pyrolysis in a plasma reactor operated with renewable electricity. In particular, the nonthermal plasma technology is promising, since energy losses are reduced, as the energy supplied is concentrated in the plasma region. In order to evaluate the application of the gliding arc plasma reactor effectively, simulations must be performed. The simulation best implemented in steps, starting with 0D, followed by 2D and finishing with 3D simulations, to investigate different aspects of the plasma reactor. The commercially available software COMSOL Multiphysics™ was used for 0D modeling of various gas mixtures, temperatures, and reaction systems. For 2D simulation of the plasma reactor the open-source OpenFOAM® was used. Its interface allows one to directly modify the integral equations describing the plasma, to monitor the progress of the solution live and to obtain results within an acceptable time range. However, it requires a demanding manual configuration of the comprehensive pertinent plasma equations and customized solvers to model the plasma successfully. For 3D simulation, several legitimate adaptations regarding plasma modeling were made. Since the prevalence of thermal effects over electron impact was revealed by 0D simulation, the plasma was replaced as a heat source. Here too, OpenFOAM® was used since the solution convergence is relatively fast. 3D simulation is also of assistance in modifying the reactor design geometry. The combination of COMSOL Multiphysics™, OpenFOAM® and Ansys Fluent® can help to facilitate the overall simulation task. In the future, it will be attempted to simulate more detailed plasma equations using just one of the simulation software options.

Supporting Information

Supporting Information for this article can be found under DOI: https://doi.org/10.1002/cite.202100181. This section includes additional references to primary literature relevant for this research [35–37].

Table 2. Software application at different levels.

Software	0D simulaton	2D simulaton	3D simulaton	Application summary
COMSOL Multiphysics™	+	±	–	Reaction set refinement
Ansys Fluent®	–	+ (with modification)	+	Fluid flow and heat transfer effects
OpenFOAM®	–	+	+	Fluid flow, heat transfer and plasma interactions

Symbols used

$a_{ij}^{((1))}$	[–]	stoichiometric coefficients
D	[–]	diffusion coefficient
E	[V]	electrical field
$f(\varepsilon_e)$	[eV^{-1}]	normalized EEDF
k_j	[cm^{3}s^{-1}; cm^{6}s^{-1}]	rate coefficient of the reaction j
m	[kg]	mass
n_l	[m^{-3}]	number density of the species on the left-hand side
q	[C]	charge
S_i	[–]	source term of species i
u_{gas}	[m s^{-1}]	gas velocity
$v(\varepsilon_e)$	[m s^{-1}]	velocity of the electrons
v_{ion}	[–]	collision frequency of the ion

Greek letters

ε_e	[eV]	electron energy
ε_{th}	[eV]	threshold energy
Γ_i	[m^{-1}s^{-1}]	electron and ion flux
μ	[V m^{-1}]	mobility

Sub- and Superscripts

i	species
j	reaction

Abbreviations

AC	alternating current
CCS	carbon capture and storage
DC	direct current
EEDF	electron energy distribution function
e	electron
GAP	gliding arc plasma
MW	microwave

References

[1] *World Energy Outlook 2020*, International Energy Agency, Paris **2020**. www.iea.org/reports/world-energy-outlook-2020

[2] *Global Energy Statistical Yearbook 2021*, Enerdata, Grenoble **2021**. https://yearbook.enerdata.net/natural-gas/world-natural-gas-production-statistics.html

[3] N. Sánchez-Bastardo, R. Schlögl, H. Ruland, *Chem. Ing. Tech.* **2020**, *92 (10)*, 1596–1609. DOI: https://doi.org/10.1002/cite.202000029

[4] *Eine kleine Wasserstoff-Farbenlehre*, Bundesministerium für Bildung und Forschung, Berlin **2020**. www.bmbf.de/bmbf/shareddocs/kurzmeldungen/de/eine-kleine-wasserstoff-farbenlehre

[5] M. Bui, C. S. Adjiman, A. Bardow, E. J. Anthony, A. Boston, S. Brown, P. S. Fennell, S. Fuss, A. Galindo, L. A. Hackett, J. P. Hallett, *Energy Environ. Sci.* **2018**, *11 (5)*, 1062–1176. DOI: https://doi.org/10.1039/C7EE02342A

[6] M. Garduño, M. Pacheco, J. Pacheco, R. Valdivia, A. Santana, B. Lefort, N. Estrada, C. Rivera-Rodríguez, *J. Renewable Sustainable Energy* **2012**, *4 (2)*, 021202. DOI: https://doi.org/10.1063/1.3663876

[7] A. Von Keudell, V. Schulz-Von Der Gathen, *Plasma Sources Sci. Technol.* **2017**, *26 (11)*, 113001. DOI: https://doi.org/10.1088/1361-6595/aa8d4c

[8] H. Conrads, M. Schmidt, *Plasma Sources Sci. Technol.* **2000**, *9 (4)*, 441. DOI: https://doi.org/10.1088/0963-0252/9/4/301

[9] Z. B. Wang, G. X. Chen, Z. Wang, N. Ge, H. P. Li, C. Y. Bao, *J. Appl. Phys.* **2011**, *110 (3)*, 033308. DOI: https://doi.org/10.1063/1.3622148

[10] A. Fridman, *Plasma Chemistry*, Cambridge University Press, Cambridge **2008**.

[11] G. Trenchev, *J. Phys. Chem.* **2017**, *121 (44)*, 24470–24479. DOI: https://doi.org/10.1021/acs.jpcc.7b08511

[12] T. Li, C. Rehmet, Y. Cheng, Y. Jin, Y. Cheng, *Plasma Chem. Plasma Process.* **2017**, *37 (4)*, 1033–1049. DOI: https://doi.org/10.1007/s11090-017-9806-x

[13] J. Meichsner, *Low Temperature Plasmas, Plasma Physics. Confinement, Transport and Collective Effects* (Eds: A. Dinklage, T. Klinger, G. Marx), Springer-Verlag, Berlin **2005**, 95–116.

[14] M. Scapinello, E. Delikonstantis, G. D. Stefanidis, *Chem. Eng. Process.* **2017**, *117*, 120–140. DOI: https://doi.org/10.1016/j.cep.2017.03.024

[15] U. Stroth, *Plasmaphysik*, Vieweg+Teubner, Wiesbaden **2011**.

[16] S. Heijkers, M. Aghaei, A. Bogaerts, *J. Phys. Chem. C* **2020**, *124 (13)*, 7016–7030. DOI: https://doi.org/10.1021/acs.jpcc.0c00082

[17] H. Zhang, W. Wang, X. Li, L. Han, M. Yan, Y. Zhong, X. Tu, *Chem. Eng. J.* **2018**, *345*, 67–78. DOI: https://doi.org/10.1016/j.cej.2018.03.123

[18] S. Kolev, A. Bogaerts, *Plasma Sources Sci. Technol.* **2014**, *24*, 015025. DOI: https://doi.org/10.1088/0963-0252/24/1/015025

[19] G. Trenchev, S. Kolev, A. Bogaerts, *Plasma Sources Sci. Technol.* **2016**, *25*, 035014. DOI: https://doi.org/10.1088/0963-0252/25/3/035014

[20] B. Sun, D. Liu, A. Yang, M. Rong, X. Wang, *Phys. Plasmas* **2019**, *26 (12)*, 123508. DOI: https://doi.org/10.1063/1.5124023

[21] www.lxcat.net

[22] I. B. Denysenko, S. Xu, J. D. Long, P. P. Rutkevych, N. A. Azarenkov, K. Ostrikov, *J. Appl. Phys.* **2004**, *95 (5)*, 2713. DOI: https://doi.org/10.1063/1.1642762

[23] R. K. Janev, D. Reitera, *Phys. Plasmas* **2002**, *9 (9)*, 4071. DOI: https://doi.org/10.1063/1.1500735

[24] R. J. Shul, R. Passarella, X. L. Yang, R. G. Keesee, A. W. Castleman, *J. Chem. Phys.* **1987**, *87 (3)*, 1630. DOI: https://doi.org/10.1063/1.453224

[25] Database Morgan (C2H6,C2H2,C2H4,CH2,CH3). www.lxcat.net

[26] D. A. Ariskin, I. V. Schweigert, *J. Exp. Theor. Phys.* **2009**, *109 (4)*, 707–716. DOI: https://doi.org/10.1134/S1063776109100173

[27] V. Nehra, A. Kumar, H. K. Dwivedi, *Int. J. Eng.* **2008**, *2 (1)*, 53–68.

[28] J. C. Legrand, A. M. Diamy, R. Hrach, V. Hrachova, *Contrib. Plasma Phys.* **1997**, *37 (6)*, 521–537. DOI: https://doi.org/10.1002/ctpp.2150370606

[29] A. Indarto, J. W. Choi, H. Lee, H. K. Song, *J. Nat. Gas Chem.* **2005**, *14*, 13–21.

[30] H. G. Weller, G. Tabor, H. Jasak, C. Fureby, *Comput. Phys.* **1998**, *12 (6)*, 620. DOI: https://doi.org/10.1063/1.168744

[31] L. L. Alves, A. Bogaerts, V. Guerra, M. M. Turner, *Plasma Sources Sci. Technol.* **2018**, *27 (2)*, 023002. DOI: https://doi.org/10.1088/1361-6595/aaa86d

[32] M. A. Lieberman, A. J. Lichtenberg, *Principles of Plasma Discharges and Materials Processing*, 2nd ed., John Wiley & Sons, Hoboken, NJ **2005**. DOI: https://doi.org/10.1002/0471724254

[33] S. Li, J. A. Medrano, V. Hessel, F. Gallucci, *Processes* **2018**, *6 (12)*, 248. DOI: https://doi.org/10.3390/pr6120248

[34] S. Böddeker et al. *Plasma Sources Sci. Technol.* **2020**, *29*, 08LT01. DOI: https://doi.org/10.1088/1361-6595/aba6a4

[35] G. J. M. Hagelaar, L. C. Pitchford, *Plasma Sci. Sources Technol.* **2005**, *14 (4)*, 722–733. DOI: https://doi.org/10.1088/0963-0252/14/4/011

[36] A. V. Phelps, *J. Res. Natl. Inst. Stand. Technol.* **1990**, *95 (4)*, 407–431. DOI: https://doi.org/10.6028/jres.095.035

[37] J. C. Legrand, A. M. Diamy, R. Hrach, V. Hrachová, *Vacuum* **1998**, *50 (3–4)*, 491–495. DOI: https://doi.org/10.1016/S0042-207X(98)00085-2